Ratio Limits of Water Storage and Outflow in Rainfall-runoff Process

Yulong Zhu[a], Yang Zhou[b], Xiaorong Xu[c], Changqing Meng[d], and Yuankun Wang[e*]

[a]**Yulong Zhu**

School of Water Resources and Hydropower Engineering, North China Electric Power University, Changping Beinong 2# 102206, Beijing, China. Email: zhuyulong@ncepu.edu.cn

[b]**Yang Zhou**

School of Water Resources and Hydropower Engineering, North China Electric Power University, Changping Beinong 2# 102206, Beijing, China. Email: zhouyang@ncepu.edu.cn

[c]**Xiaorong Xu**

School of Water Resources and Hydropower Engineering, North China Electric Power University, Changping Beinong 2# 102206, Beijing, China. Email: xxrong@ncepu.edu.cn

[d]**Changqing Meng**

School of Water Resources and Hydropower Engineering, North China Electric Power University, Changping Beinong 2# 102206, Beijing, China. Email: els_meng@ncepu.edu.cn

[e*]**Yuankun Wang** (Corresponding author)

School of Water Resources and Hydropower Engineering, North China Electric Power University, Changping Beinong 2# 102206, Beijing, China. Email: yuankunw@ncepu.edu.cn

Abstract

Flash floods typically occur suddenly within hours of heavy rainfall. Accurate forecasting of flash floods in advance using the two-dimensional (2D) shallow water equations (SWEs) remains a challenge, due to the governing equations of SWEs being difficult-to-solve partial differential equations (PDEs). Aiming at shortening the computational time and gaining more time for issuing early warnings of flash floods, a new relationship between water storage and outflow in the rainfall-runoff process is attempted to be constructed by assuming the catchment as a water storage system. Through numerical simulations of the diffusion wave (DW) approximation of SWEs, the water storage and discharge are found to be limited to envelope lines, and the discharge/water depth process lines during water rising and falling showed a grid-shaped distribution. Furthermore, if a catchment is regarded as a semi-open water storage system, there is a nonlinear relationship between the inside average water depth and the outlet water depth, namely the water storage ratio curve, which resembles the shape of a "plume". In the case of an open channel without considering spatial variability, the water storage ratio curve is limited to three values (i.e. the upper, the steady, and the lower limit), which are found to be independent of meteorological (rainfall intensity), vegetation (Manning's coefficient), and terrain (slope gradient) conditions. Meteorological, vegetation, and terrain conditions only affect the size of the "plume" without changing its shape. Rainfall, especially weak rain (i.e. when rainfall intensity is less than 5.0 mm h^{-1}) significantly affects the fluctuations of the water storage ratio, which can be divided into three modes, that is Mode I (inverse S-shape type) during the rainfall beginning stage, Mode II (wave type) during the rainfall duration stage, and Mode III (checkmark type) during rainfall end stage. Results indicate that the determination of the nonlinear relationship of the water storage ratio curve under different geographical scenarios will provide new ideas for simulation and early warning of flash floods.

1. Introduction

Flood disaster is a significant global health and economic threat. Disastrous floods have caused millions of fatalities in the twentieth century and billions of dollars in direct economic losses each year (Merkuryeva et al., 2015; Merz et al., 2021; Ruidas et al., 2022). According to statistics (Lee et al., 2020), from 2001 to 2018, over 2,900 floods caused over 93,000 deaths and over 490 billion USD in economic damages worldwide. Based on 250-meter resolution daily satellite images of 913 major flood events during the same period, the total area inundated by floods is estimated to be 2.23 million km^2 and the directly affected population is estimated to be 255 to 290 million (Tellman et al., 2021). With the influence of climate change and extreme El Niño events (Ward et al., 2014; Cai et al., 2014), flood events caused by extreme precipitation are occurring frequently in many regions around the world (Kirezci et al., 2020; Najibi and Devineni, 2018; Almazroui, 2020). From 2020 to 2023, catastrophic floods caused by several extreme rainfall events were reported in Germany (Tradowsky et al., 2023), China (Hsu et al., 2021), Italy (Valente et al., 2023), Japan (Kobayashi et al., 2023), Pakistan (Nanditha et al., 2023) and other developed or developing countries and regions, even in some desert areas, e.g. in the Taklimakan Desert and the Atacama Desert, as reported by Li and Yao (2023) and by Cabré et al. (2023) respectively. Research show that under a high emissions scenario, in latitudes above 40^o north, compound flooding could become more than 2.5 times as frequent by 2100 compared to the present (Bevacqua et al., 2020). It means that in the future, the fraction of the global population at risk of floods will be growing.

Flood simulation provides an effective means of flood forecasting to reduce property and life losses in flood-threatened areas around the world. Particularly, weather prediction-based distributed hydrological/hydraulic models are considered to be an effective strategy for flood simulation (Ming et al., 2020). Hence, a large number of scholars are committed to improving the simulation efficiency or simulation

accuracy of distributed hydrological/hydraulic models. Accordingly, they have developed many forms of hydrological models and hydrodynamic models in the past decades. Among them, the hydrological models include Stanford Watershed Model IV-SWM (Crawford and Linsley, 1966), SHE/MIKESHE model (Abbott et al., 1986), Tank model (Sugawara, 1995), Soil and Water Assessment Tool-SWAT (Arnold and Williams, 1987), and TOPMODEL (Beven and Kirkby, 1979). The hydrodynamic models include the one-dimensional (1D) Saint-Venant equation (Köhne et al., 2011), the two-dimensional (2D) SWEs (Camassa et al., 1994), and the three-dimensional (3D) integrated equations of runoff and seepage (Mori et al., 2015). In addition, a variety of hydrological-hydrodynamic coupling models have also been proposed by Kim et al. (2012), Liu et al. (2019), Hoch et al. (2019), and other scholars. Particularly, SWEs are the main governing equations for simulating floods. However, flood simulation based on SWEs is a time-consuming process due to its governing equations being a hyperbolic system of first-order nonlinear partial differential equations (PDEs) (Li and Fan, 2017). Therefore, many scholars attempted to improve the efficiency and accuracy of flood simulation through computer technology e.g. applying GPU parallel computing (Crossley et al., 2010) or advanced numerical scheme (Sanders et al., 2010). For hydrological studies, the performance of hydrological modeling is usually challenged by model calibration and uncertainty analysis during modeling exercises (Wu et al., 2021).

Efficient and stable solution of the hydrodynamic model has long been an important issue in flood forecasting. Since the SWEs are nonlinear hyperbolic PDEs, the increase in the calculation domain and the increase in the degree of discreteness will greatly increase the difficulty of solving SWEs. In addition, when using high-resolution terrain to improve model calculation accuracy, non-physical phenomena such as false high flow velocity in steep terrain will also occur, resulting in calculation distortion and a sharp increase in calculation time. Hence, we try to ignore the complex exchange/transfer process of mass and momentum

(hydrodynamic models), and also abandon the empirical relationships (hydrological models) between the input (precipitation), the transmission (flow rate), and the output (discharge) in the catchment area. A catchment is regarded as a semi-open water storage system, and the complex problem is simplified into three megascopic variables, i.e. inflow, water storage, and outflow. For one watershed, the complex internal flow processes could be ignored if the physical mechanism between inflow, water storage, and outflow can be found under different meteorological, geographical, and geological conditions. In other words, if we can give a physical-based relationship between the three megascopic variables, flood forecasting will become much simpler.

2. Methods

An arbitrary catchment (Fig. 1b) could be assumed to be a conceptual water tank (Fig. 1a). In this water tank, according to the law of conservation of mass, the complex confluence process of surface runoff could be neglected and it can be described only by the relationship between input, storage and output, which can be expressed as Eq. 1,

$$\underbrace{A \times \frac{dH}{dt}}_{storage} = \underbrace{R \times A}_{rainfall} - \underbrace{I \times A}_{\text{infiltration}} + \underbrace{F \times A}_{exfiltration} - \underbrace{E \times A}_{\text{evaporation}} - \underbrace{\frac{Q}{A} \times A}_{discharge} \quad (1)$$

where A is catchment area (m^2); t is time (s); H is internal average water depth (m); R is rainfall intensity ($m\ s^{-1}$); I is infiltration ($m\ s^{-1}$); F is exfiltration ($m\ s^{-1}$); E is evaporation ($m\ s^{-1}$) and Q is discharge ($m^3\ s^{-1}$).

In this section, attentions are focused on the surface flow of runoff, so the runoff-atmosphere moisture exchange (evaporation) and runoff-soil moisture exchange (infiltration and/or exfiltration) are non-considered. Zhu et al. (2020) validated the effectiveness of a diffusion wave (DW) approximation of shallow water equations by numerical simulations for simulating ground surface runoff,

$$\frac{\partial h}{\partial t} - \nabla\left(\frac{h^{5/3}}{n_m\sqrt{|S|}}\nabla(h+z)\right) = R \tag{2}$$

where h is water depth (m); z is elevation (m); n_m is Manning's coefficient (s $m^{-1/3}$) and S is the slope gradient.

To improve the computational efficiency of the hydrodynamic model, after strict mathematical derivation according to the basic hydrodynamic equation and the law of conservation of mass, Zhu et al. (2022) proposed a hydrological-hydrodynamic integrated model, i.e. distributed runoff model (DRM) as,

$$\begin{cases} \frac{dH}{dt} = R - q \\ H = \eta h = \eta\left(\frac{n_m}{\sqrt{S}}\right)^{0.6} q^{0.6}\left(\frac{A}{B}\right)^{0.6} \end{cases} \tag{3}$$

where $q=Q/A$ is conceptual outflow (m s^{-1}); η is the water storage ratio; B is the outlet width (m).

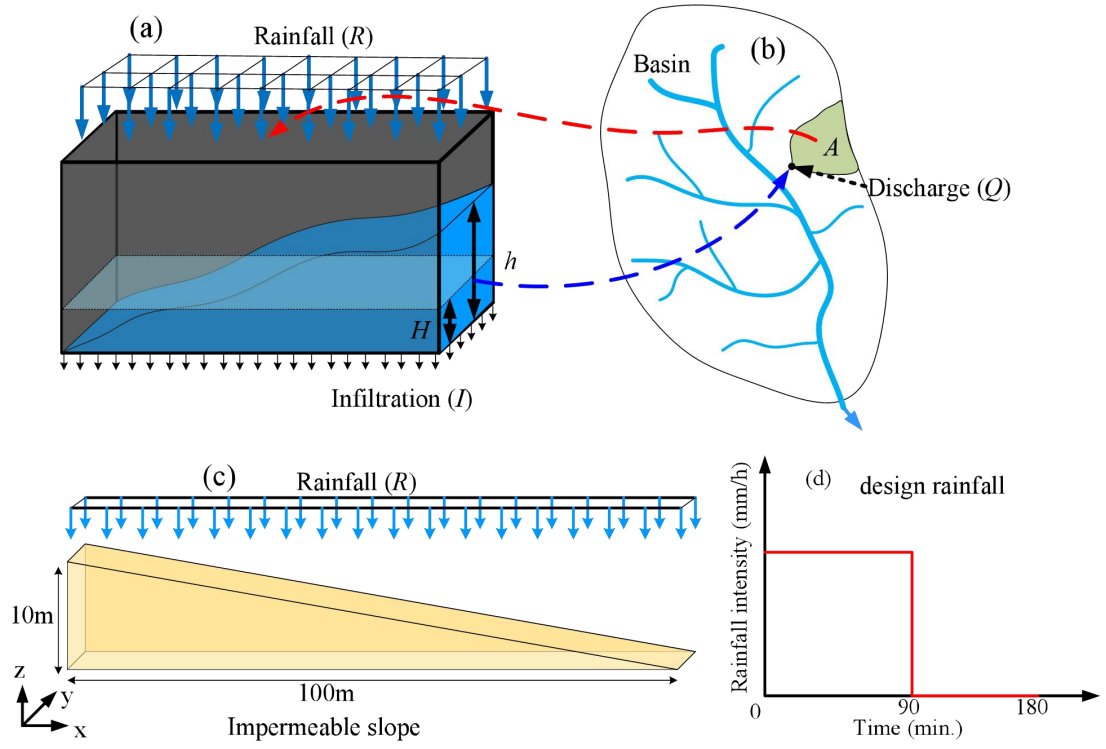

Fig. 1. Conceptual schematic of the DRM and numerical model. (a) conceptual water tank; (b) conceptual catchment; (c) impermeable conceptual slope model; (d) design rainfall.

3. Limits and "plume" shape of water storage ratio curve

The conceptual hydrological model takes the inside average water depth (H) in the catchment area as

the independent variable (Eq. 1). However, the hydrodynamic equations take the water depth at any outlet (h) as an independent variable (Eq. 2). If a relationship between the inside average water depth (H) and outlet water depth (h) can be established, then this relationship will have both hydrodynamic and hydrological characteristics. Therefore, to find the H-h relationship, an impermeable conceptual slope model was built as shown in Fig. 1c, and numerical simulations were performed using diffusion wave (DW) approximation (Eq. 2) of shallow water equations (SWEs). The water storage ratio is defined as the inside average water depth (H) divided by the outlet water depth (h). Firstly, the numerical simulations are performed under a designed rainfall condition, i.e. rainfall intensity is 10 mm h^{-1} and rainfall duration is 90 minutes with a total time of 180 minutes as shown in Fig. 1d. From the time-dependent water storage ratio (H/h) under different catchment area (Fig. 2a), it can be seen that the continuous rainfall will cause the water storage ratio (H/h) to gradually decrease from the initial value 1.0 (upper limit) to a stable value, which is approximately 0.625 (steady limit). When the rainfall ends, the value of the water storage ratio (H/h) decreases first and then increases, showing a U-shaped curve with a lower limit, which is approximately 0.4125. Afterward, the water storage ratio curves under ten kinds of catchment area (Fig. 2b), three kinds of Manning's coefficient (Fig. 2c), four kinds of slope gradient (Fig. 2d), and four kinds of rainfall intensity (Fig. 2e) conditions are obtained from parametric analyses and collected in Fig. 2f.

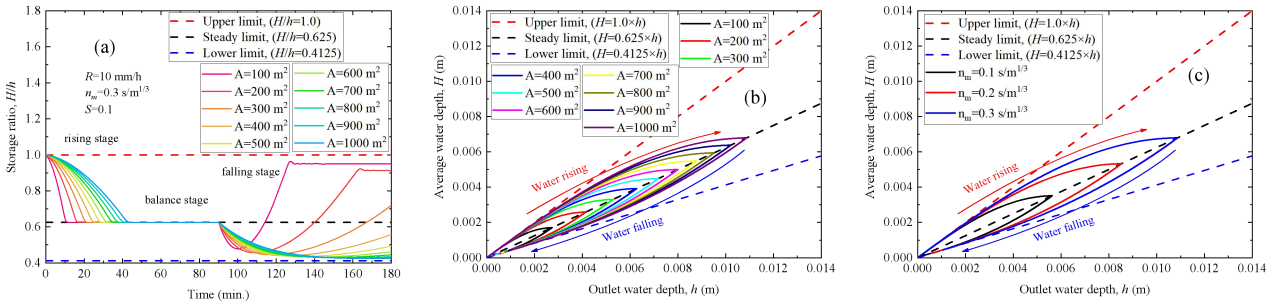

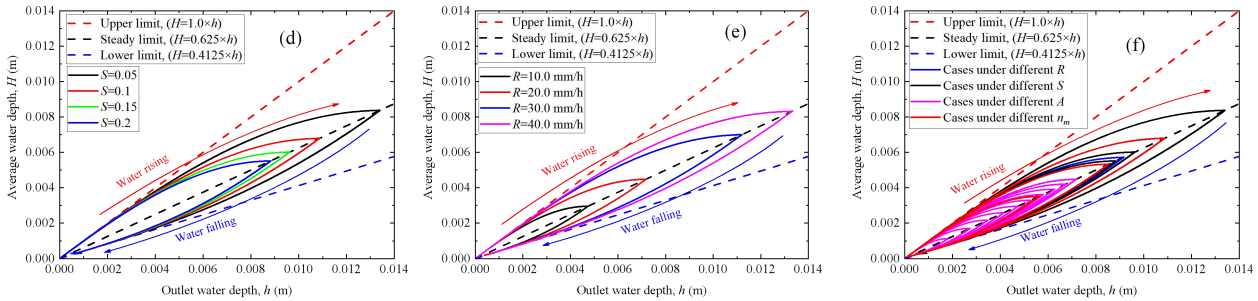

138

139 **Fig. 2. Water storage ratio curves**. (a) time-dependent water storage ratio under different catchment

140 areas with 10 mm h^{-1}; (b) water storage ratio curves under ten kinds of catchment area; (c) water storage ratio

141 curves under three kinds of Manning's coefficient; (d) water storage ratio curves under four kinds of slope

142 gradient; (e) water storage ratio curves under four kinds of rainfall intensity; (f) collection of the above

143 twenty one water storage ratio curves. Three limit lines envelop all water storage ratio curves, i.e. upper limit

144 (H/h=1.0), steady limit (H/h=0.625), and lower limit (H/h=0.4125).

145 Finally, it is found that water storage ratio curves resemble the shape of a "plume". When the water

146 outlet depth is the same, the water storage ratio (H/h) of the water-rising limb is higher than that of the

147 water-falling limb. Furthermore, in the case of an open channel without considering spatial variability, there

148 are three limits (the upper, the steady, and the lower limit) of the water storage ratio curves, which are found

149 to be independent of meteorological (rainfall intensity), vegetation (Manning's coefficient), and terrain (slope

150 gradient) conditions. Meteorological, vegetation, and terrain conditions only affect the size of the "plume"

151 without changing its shape which is anchored by three limits. This means that the three limits and the water

152 storage ratio curves provide a key to establishing a relationship between the hydrodynamic models and the

153 hydrological models.

154 **4. Grid-shaped cross-distribution of discharge/water depth process lines during water rising and**

155 **falling**

156 To obtain further insights into the causes for the formation of the water-rising limb and the water-falling

limb of the water storage ratio curve, the ratio of discharge (i.e. the ratio of the total outflows (Q_{out}) to the total inflows (Q_{in})), and the water depth (h) along the slope are discussed in Fig. 3a and Fig. 3d, respectively. Results indicate that there is an envelope line that controls the distribution of the discharge and water depth along the slope, respectively. The discharge envelope line is a straight line with a slope of 1% (Fig. 3a), while the water depth envelope line is a nonlinear curve controlled by a power function of general form $h=kx^a$ (Fig. 3d). It means that if the duration of rainfall with a constant intensity is long enough, the catchment system will eventually reach an equilibrium state between inflow and outflow.

On the other hand, the process lines of discharge and water depth during water rising and falling present a grid-shaped cross-distribution (Fig. 3a and Fig. 3d). Similarly, from the view of the gradient of the discharge and water depth process lines during water rising and falling, the discharge gradient curves (Fig. 3b) and the water depth gradient curves (Fig. 3e) also present a grid-shaped cross-distribution during water rising and falling, which might be the cause of the looped rating curve (Fig. 3c), i.e. higher discharges for the rising limb (Q_u) than for the recession limb (Q_f) at the same stage (Petersen-Øverleir, 2006). After fitting the value of parameter k and a under different rainfall intensity (R), Manning's coefficient (n_m), and slope gradient (S) conditions (Fig. 3f), it is found that the parameter a is a constant, while the change of parameter k is positively correlated with the change of rainfall intensity (R) and Manning's coefficient (n_m), but negatively correlated with the change of slope gradient (S).

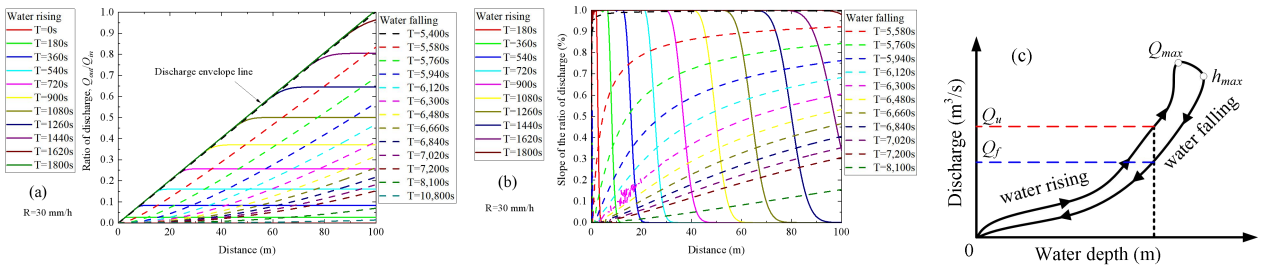

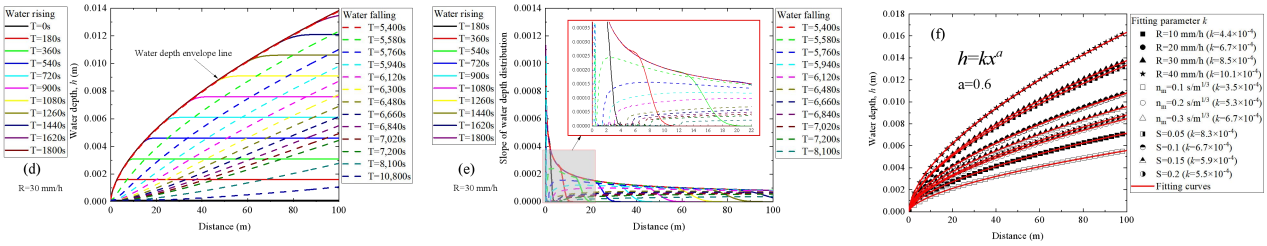

Fig. 3. Discharge/water depth process lines during water rising and falling. (a) discharge process lines during water rising and falling; (b) gradient lines of discharge process line during water rising and falling; (c) schematic diagram of looped rating curve; (d) water depth process lines during water rising and falling; (e) gradient lines of water depth process lines during water rising and falling; (f) change of water depth envelope line under different rainfall intensity (R), Manning's coefficient (n_m), and slope gradient (S).

Based on the water storage ratio curve, a hydrological-hydrodynamic integrated model, namely the Distributed Runoff Model (DRM), is established with the governing equations in Eq. 3. To check the effectiveness and applicability of DRM, a comparative analysis of the numerical results obtained from the DRM and the DW model is implemented. We found that the DRM quickly reproduces the calculation results of the time-consuming DW model under different rainfall intensities (Fig. 4a and Fig. 4b), different Manning's coefficients (Fig. 4c), and different slope gradients (Fig. 4d). meaning that the water storage ratio curve will provide new ideas for simulation and early warning of floods. In addition, due to the governing equations of DRM being an ordinary differential equations (ODEs), the computational efficiency of DRM is much higher than the DW model, which is governed by nonlinear partial differential equations (PDEs). More attention should be paid to the determination of the nonlinear relationship of the water storage ratio curve under different geographical scenarios, which will be beneficial to the proposal of more efficient flood forecasting methods or early warning systems.

193

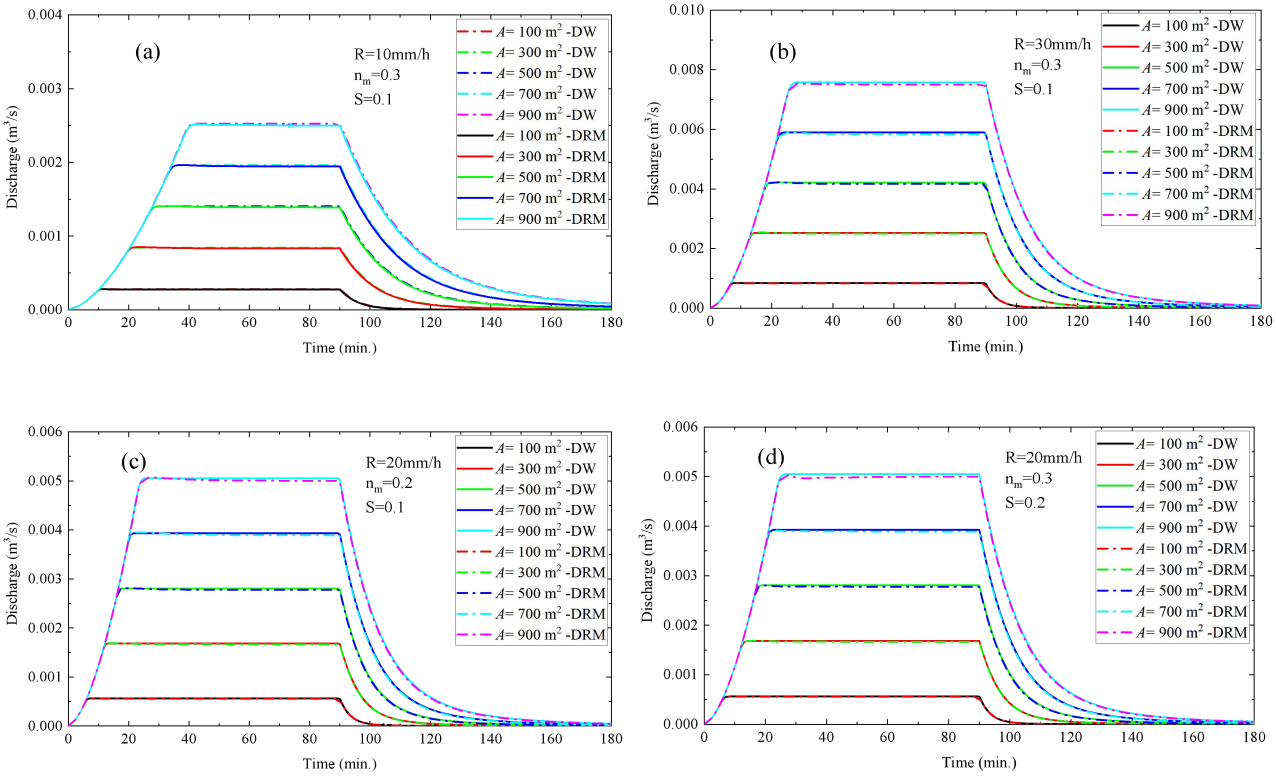

194

195 **Fig. 4. Comparative analyses of discharge calculated by DW and DRM under designed rainfall**. (a)

196 controlled group; (b) compared with (a), only the rainfall intensity is changed; (c) compared with (a), rainfall

197 intensity and Manning coefficient are changed; (d) compared with (a), rainfall intensity and slope gradient

198 are changed.

199 **5. Validation of DRM by considering infiltration calculated by Horton infiltration method.**

200 In the above section, the simulations of DW and DRM are based on an impermeable conceptual slope

201 model as shown in Fig. 1c. After considering infiltration in the DW and DRM, Eq. 2 and Eq. 3 become:

202 $$\frac{\partial h}{\partial t} - \nabla\left(\frac{h^{\frac{5}{3}}}{n_m\sqrt{|S|}}\nabla(h+z)\right) = R - I \tag{4}$$

203 $$\begin{cases} \frac{dH}{dt} = R - q - I \\ H = \eta h = \eta\left(\frac{n_m}{\sqrt{S}}\right)^{0.6} q^{0.6}\left(\frac{A}{B}\right)^{0.6} \end{cases} \tag{5}$$

204 Infiltration (I) is calculated by Horton's infiltration model (Horton, 1933), which suggests an

205 exponential equation for modeling the soil infiltration capacity f_p (m s^{-1}):

$$f_p(t) = f_c + (f_0 - f_c)e^{-kt} \quad (6)$$

where f_0 is the initial infiltration capacity (m s^{-1}), f_c is the final infiltration capacity (m s^{-1}), k represents the rate of decrease in the capacity (s^{-1}). The infiltration parameter sets are listed in Table 1.

Table 1 Infiltration parameter sets.

Parameter	k (s^{-1})	f_c (m s^{-1})	f_0 (m s^{-1})
Value	2.43×10^{-3}	3.272×10^{-5}	1.977×10^{-4}

A rainfall event begins with a weak precipitation intensity. When the rainfall intensity is less than the infiltration capacity, all the rainwater will infiltrate into the soil. While, when the rainfall intensity exceeds the soil infiltration capacity, the surface water is generated, and Horton law (Eq. 6) applies:

$$I = \begin{cases} R(t) & \text{if } R(t) \le f_p(t) \\ f_p(t) & \text{if } R(t) > f_p(t) \end{cases} \quad (7)$$

Results of outlet discharge (Q) and runoff volume (ROV) calculated by DW and DRM are compared with the reference results adopted from Fernández-Pato et al. (2016) as shown in Fig. 5. Fig. 5a shows the comparison of results under a uniform design rainfall. In this case, the rain volume is 75,000 m^3 with a duration of 250 minutes (min.). Fig. 5b shows the comparison of results under a non-uniform rainfall. Rain volume is 75,000 m^3 with a duration of 250 minutes (min.). From Fig. 5, it can be recognized that after considering infiltration, except that the calculation results of DRM are a little small at the end-stage of rainfall, the calculation results of DRM are still highly consistent with the calculation results of the DW model and reference results adopted from Fernández-Pato et al. (2016).

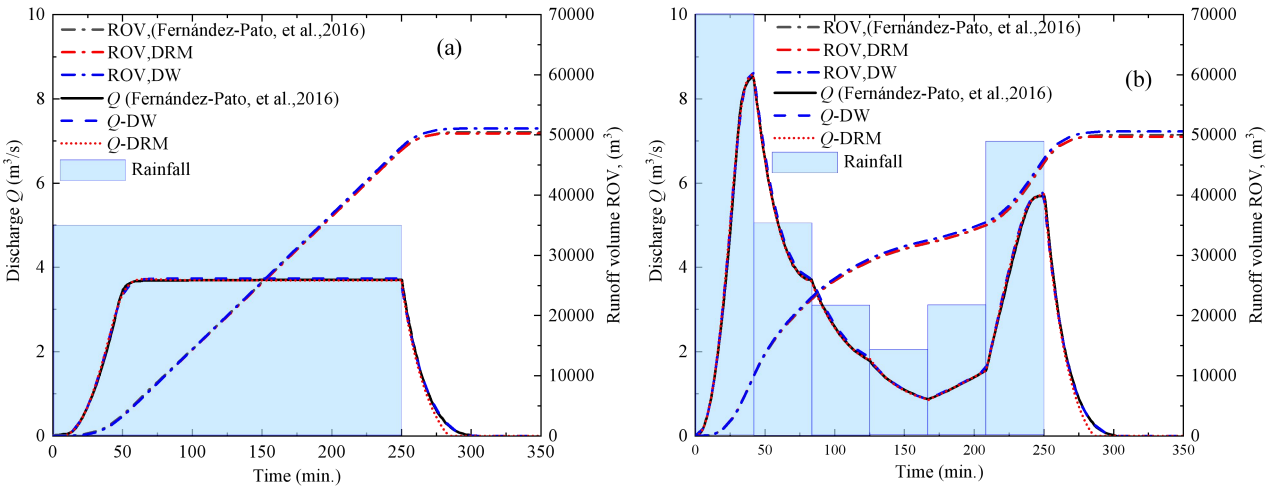

Fig. 5. Outlet discharge (*Q*) and runoff volume (ROV) calculated by DW and DRM vs. reference results adopted from Fernández-Pato et al. (2016).

6. Fluctuation of water storage ratio under natural rainfall conditions

After implementing a real rainfall event in the impermeable conceptual slope model (Fig. 1c), the change of the water storage ratio is calculated as shown in Fig. 6. Rainfall data was recorded from 09 August 2022 00:00 to 10 August 2022 00:00 in Aomori Prefecture, Japan and from 29 August 2016 01:00 to 31 August 2016 09:00 in Nissho Pass, Japan (https://www.data.jma.go.jp). The total simulation time is 30 hours and 56 hours, respectively. Results show that in addition to the fluctuations of water storage ratio in the beginning and end stages of rainfall, there are mainly ten fluctuation periods of water storage ratio during the rainfall duration stage, identified as $1^{\#}$, $2^{\#}$, $3^{\#}$, $4^{\#}$, and $5^{\#}$ in Fig. 6a and $6^{\#}$, $7^{\#}$, $8^{\#}$, $9^{\#}$, and $10^{\#}$ in Fig. 6b. The fluctuations are found to be mainly caused by weak rainfall (i.e. rainfall intensity is near 5.0 mm h^{-1}) as pointed by the red arrows in Fig. 6a and Fig. 6b. The magnitude of the fluctuations appears to be positively correlated with the difference between rainfall intensity and 5.0 mm h^{-1}. When the rainfall intensity continues to be greater than 5.0 mm h^{-1}, the fluctuation of the water storage ratio is not obvious. The water storage ratio is stable near the steady limit, even if there is heavy rainfall during this period.

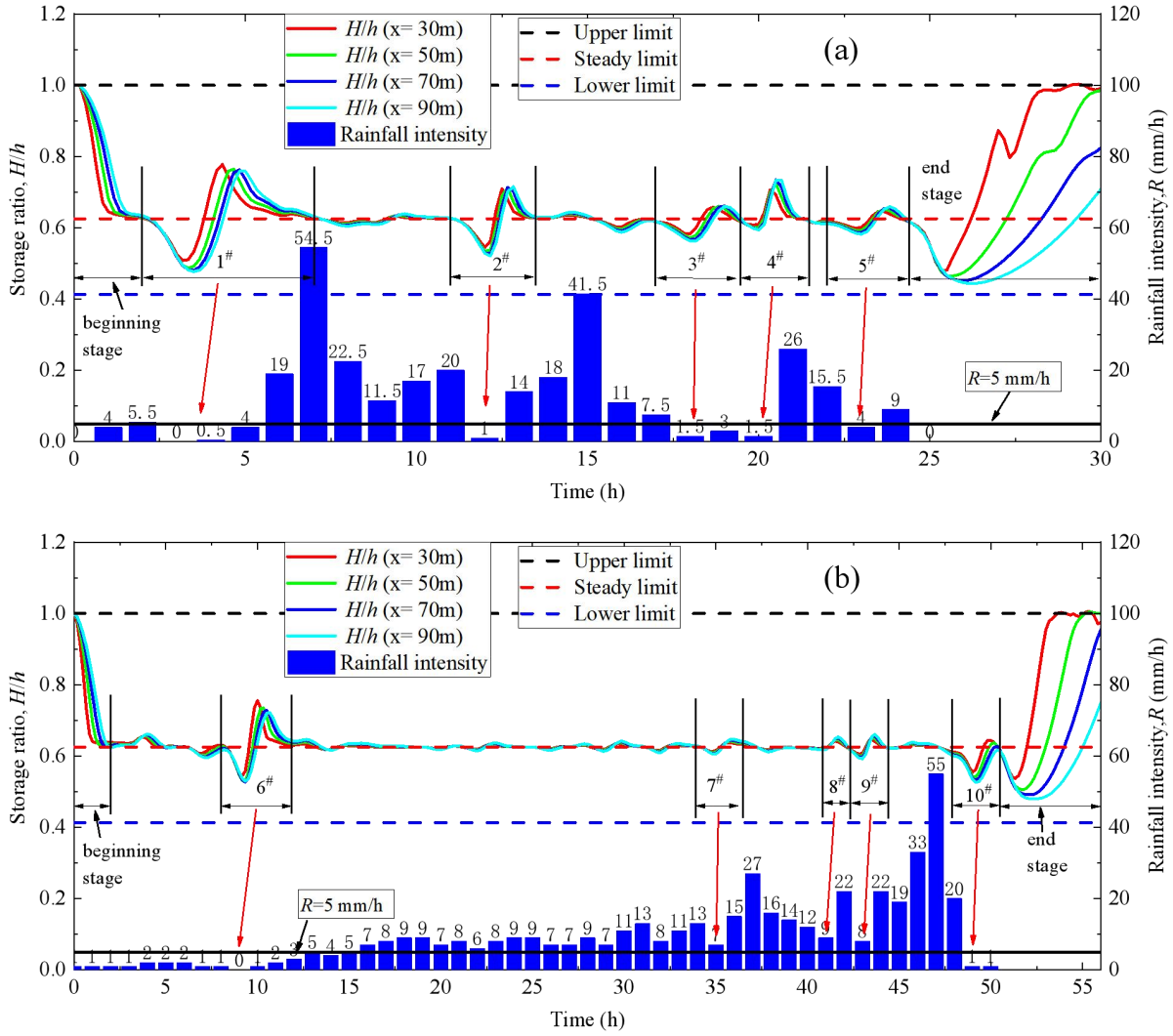

Fig. 6. The fluctuation of water storage ratio and the effectiveness of DRM in natural rainfall events. (a) Aomori Prefecture; (b) Nissho Pass.

Besides, the fluctuations of the water storage ratio can be divided into three modes, that is Mode I identified as the inverse S-shape type during the rainfall beginning stage (Fig. 7a), Mode II identified as wave type during the weak rainfall duration stage (Fig. 7b), and Mode III identified as checkmark type during rainfall end-stage (Fig. 7c). Among them, Mode I describes how water storage ratio drops from upper limit to steady limit in an inverse S-shape. Mode II represents the water storage fluctuations around the steady limit. Mode III happens when the water storage ratio first drops from the steady limit to the lower limit and then rises to the upper limit. This means that the certainty of the fluctuation modes will provide the

possibility for quantitative analysis of the fluctuation of the water storage ratio induced by the change in the rainfall intensity.

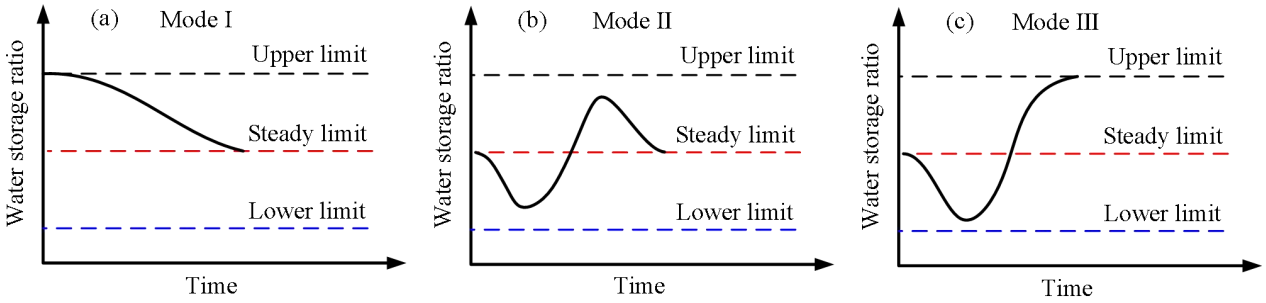

Fig. 7. Three kinds of water storage ratio fluctuation modes in natural rainfall events. (a) Mode I during the rainfall beginning stage; (b) Mode II during the weak rainfall duration stage; (c) Mode III during the rainfall end stage.

Figures 8a and 8b show the simulation results of discharge calculated by the DRM and DW model using the rainfall data recorded in Aomori Prefecture and Nissho Pass, Japan, respectively. Results suggest that after the determination of the water storage ratio fluctuations, the calculation results of DRM are in good agreement with those of the DW model, meaning that DRM provides a new and more effective theoretical scheme for flood prediction.

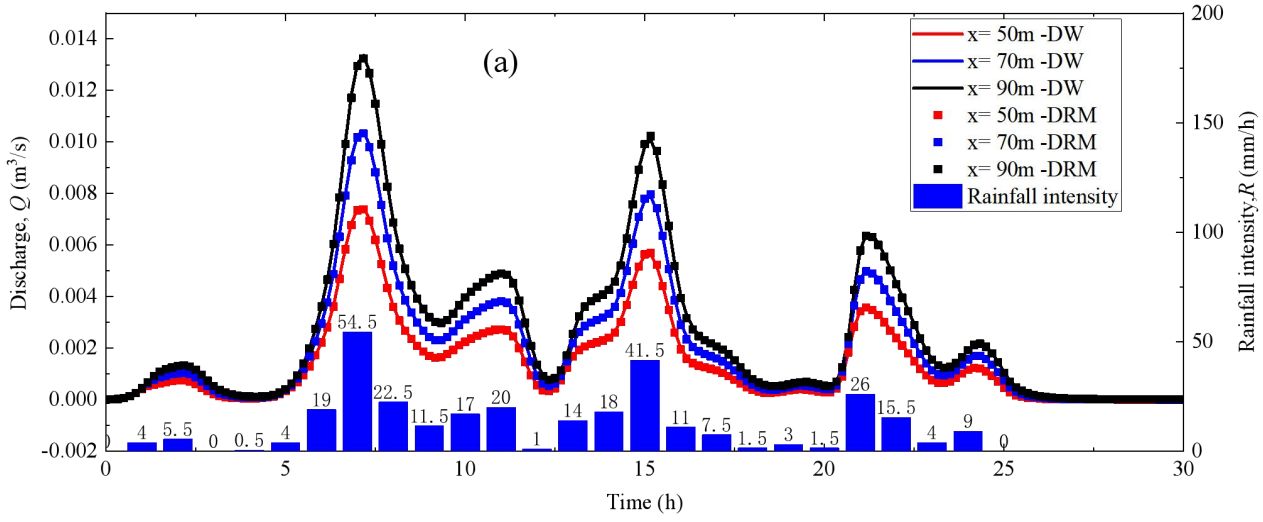

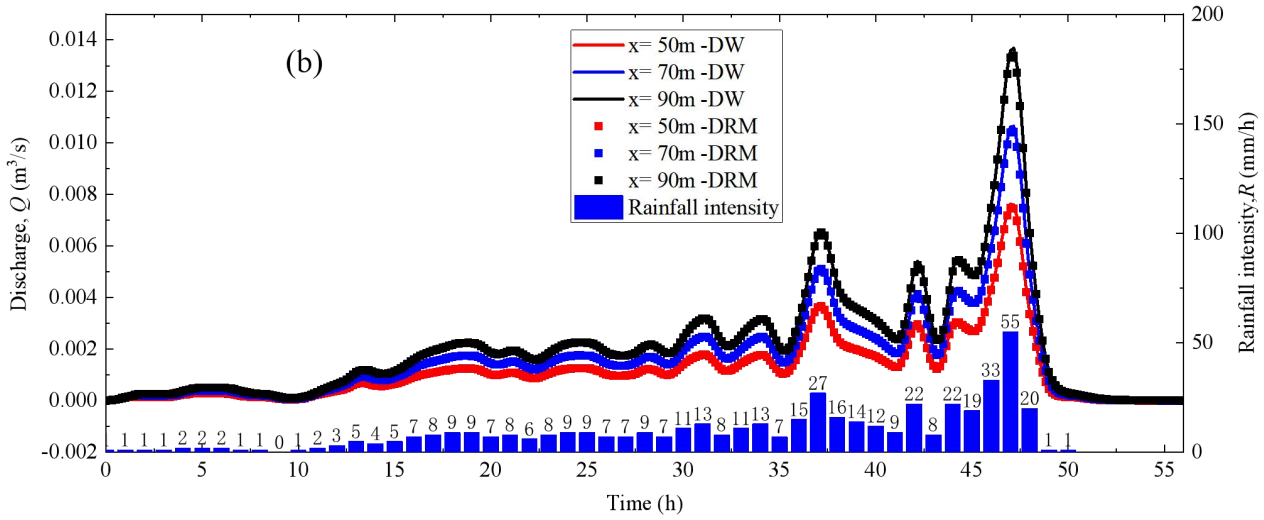

Fig. 8. Time-dependent discharge calculated by DRM and DW model. (a) Aomori Prefecture; (b) Nissho Pass.

7. Discussions and Conclusions

Based on a conceptual slope model, numerical simulations of the rainfall-runoff process are performed by using the diffusion wave (DW) approximation of SWEs. A "plume" shaped nonlinear relationship between water storage and outflow, defined as the water storage ratio, is found between the inside average water depth and the outlet water depth in a catchment. The water storage ratio is controlled by three limits, namely upper limit, steady limit, and lower limit with the value of approximately 1.0, 0.625, and 0.4125, respectively. Under the control of the three limits, meteorological, vegetation, and terrain conditions only affect the size of the "plume" without changing its shape. The regular curve shape of the water storage ratio provides the possibility to construct a correlation between the water storage in the catchment area and the outlet discharge.

Based on the water storage ratio, a hydrological-hydrodynamic integrated model (DRM), is established, which shows high calculation accuracy and computational efficiency. This is because the governing equations of DRM are ordinary differential equations (ODEs), which are much easier to solve than nonlinear

partial differential equations (PDEs). However, the calculations of DRM and DW only involve the confluence part of surface water and infiltration, while the interbasin groundwater flow as inputs to the watershed (exfiltration) and evaporation are not considered. This is inconsistent with the real rainfall-runoff process in the watershed and may lead to deviations in the calculation results. Therefore, the flow exchange between surface water and groundwater during the existence and extinction of runoff also needs to be further realized by establishing a dynamic coupling model of surface water and groundwater.

In addition, the water storage and discharge are limited to envelope lines, and the discharge/water depth process lines during water rising and falling showed a grid-shaped distribution, which might be the cause of the looped rating curve, i.e. higher discharges for the rising limb than for the recession limb at the same stage. Rainfall, especially weak rainfall (i.e. rainfall intensity less than 5.0 mm h^{-1}) significantly affects the fluctuations of the water storage ratio. The fluctuations of water storage ratio during a real rainfall event can be divided into three modes, that is Mode I identified as inverse S-shape type during the rainfall beginning stage, Mode II identified as Wave type during weak rainfall duration stage, and Mode III identified as checkmark type during rainfall end stage. It is worth noting that a qualitative determination of the three fluctuation modes of water storage ratio during rainfall events is obtained, but the quantitative analysis still needs to be further carried out in the future.

The findings in this study provide a key to establishing a simpler prediction model for flash floods. The water storage ratio has been proven to be effective in improving the effectiveness and efficiency of flood forecasting. Therefore, the determination of the nonlinear relationship of the water storage ratio curve under different geographical scenarios will provide new ideas for simulation and early warning of flash floods.

Authors' contributions

Yulong Zhu: Conceptualization, Methodology, Software, Validation, Formal Analysis, Investigation, Data

Curation, Writing-Original draft, Writing - Review & Editing.

Yang Zhou: Methodology, Validation, Investigation, Resources, Data Curation.

Xiaorong Xu: Methodology, Investigation, Data Curation.

Changqing Meng: Validation, Investigation, Data Curation.

Yuankun Wang: Conceptualization, Methodology, Writing-Original draft, Writing - Review & Editing, Supervision, Project administration, Funding acquisition.

Availability of data and materials

The datasets used and/or analyzed during the current study are available from the corresponding author on reasonable request.

Competing interests

The authors declare that they have no conflict of interest.

Acknowledgments

This study was supported by the National Natural Science Fund of China (52279064, 52209087), and the Fundamental Research Funds for the Central Universities of China (2024MS069, 2024MS068).

References

Abbott, M. B., Bathurst, J. C., Cunge, J. A., O'Connell, P. E., and Rasmussen, J.: An introduction to the European Hydrological System-Systeme Hydrologique Europeen,"SHE", 1: History and philosophy of a physically-based, distributed modelling system. Journal of Hydrology, 87(1-2), 45-59,

https://doi.org/10.1016/0022-1694(86)90114-9, 1986.

Almazroui, M.: Rainfall trends and extremes in Saudi Arabia in recent decades. Atmosphere, 11(9), 964, https://doi.org/10.3390/atmos11090964, 2020.

Arnold, J. G., and Williams, J. R.: Validation of SWRRB: Simulator for water resources in rural basins. J. Water Resour. Plan. Manage. ASCE, 113(2), 243-256, https://doi.org/10.1061/(ASCE)0733-9496(1987)113:2(243), 1987.

Beven, K. J. and Kirkby, M. J.: A Physically Based Variable Contributing Area Model of Basin Hydrology. Hydrological Sciences Bulletin, 24, 43-69, https://doi.org/10.1080/02626667909491834, 1979.

Bevacqua, E., Vousdoukas, M. I., Zappa, G., Hodges, K., Shepherd, T. G., Maraun, D., Mentaschi, L., and Feyen, L.: More meteorological events that drive compound coastal flooding are projected under climate change. Communications Earth & Environment, 1(1), 47, https://doi.org/10.1038/s43247-020-00044-z, 2020.

Cabré, A., Remy, D., Marc, O., Burrows, K., and Carretier, S.: Flash floods triggered by the 15-17th March 2022 rainstorm event in the Atacama Desert mapped from InSAR coherence time series. Natural Hazards, 116(1), 1345-1353, https://doi.org/10.1007/s11069-022-05707-y, 2023.

Cai, W., Borlace, S., Lengaigne, M., van Rensch, P., Collins, M., Vecchi, G., Timmermann, A., Santoso, A., McPhaden, M. J., Wu, L., England, M. H., Wang, G., Guilyardi, E., and Jin, F. F.: Increasing frequency of extreme El Niño events due to greenhouse warming. Nature Climate Change, 4(2), 111-116, https://doi.org/10.1038/nclimate2100, 2014.

Camassa, R., Holm, D. D., and Hyman, J. M.: A new integrable shallow water equation. Advances in Applied Mechanics, 31, 1-33, https://doi.org/10.1016/S0065-2156(08)70254-0, 1994.

Crawford, N. H. and Linsley, R. K.: Digital Simulation in Hydrology: Stanford Watershed Model IV.

344 Technical Report No. 39, Department of Civil Engineering, Stanford University, pp. 210, 1966.
345 Crossley, A., Lamb, R., Waller, S., and Dunning, P.: Fast 2D flood modelling using GPU technology-recent
346 applications and new developments. In EGU General Assembly Conference Abstracts, p. 12043, 2010.
347 Fernández-Pato, J., Caviedes-Voullième, D., and García-Navarro, P.: Rainfall/runoff simulation with 2D full
348 shallow water equations: Sensitivity analysis and calibration of infiltration parameters. Journal of
349 hydrology, 536, 496-513, https://doi.org/10.1016/j.jhydrol.2016.03.021, 2016.
350 Hoch, J. M., Eilander, D., Ikeuchi, H., Baart, F., and Winsemius, H. C.: Evaluating the impact of model
351 complexity on flood wave propagation and inundation extent with a hydrologic–hydrodynamic model
352 coupling framework. Natural Hazards and Earth System Sciences, 19(8), 1723-1735,
353 https://doi.org/10.5194/nhess-19-1723-2019, 2019.
354 Horton, R.: The role of infiltration in the hydrologic cycle. Trans. Am. Geophys. Union 14, 446-460,
355 https://doi.org/10.1029/TR014i001p00446, 1933.
356 Hsu, P. C., Xie, J., Lee, J. Y., Zhu, Z., Li, Y., Chen, B., and Zhang, S.: Multiscale interactions driving the
357 devastating floods in Henan Province, China during July 2021. Weather and Climate Extremes, 39,
358 100541, https://doi.org/10.1016/j.wace.2022.100541, 2023.
359 Kim, J., Warnock, A., Ivanov, V. Y., and Katopodes, N. D.: Coupled modeling of hydrologic and
360 hydrodynamic processes including overland and channel flow. Advances in Water Resources, 37,
361 104-126, https://doi.org/10.1016/j.advwatres.2011.11.009, 2012.
362 Kirezci, E., Young, I. R., Ranasinghe, R., Muis, S., Nicholls, R. J., Lincke, D., and Hinkel, J.: Projections of
363 global-scale extreme sea levels and resulting episodic coastal flooding over the 21st Century. Scientific
364 Reports, 10(1), 11629, https://doi.org/10.1038/s41598-020-67736-6, 2020.
365 Kobayashi, K., Duc, L., Kawabata, T., Tamura, A., Oizumi, T., Saito, K., Nohara, D., and Sumi, T.: Ensemble

366 rainfall–runoff and inundation simulations using 100 and 1000 member rainfalls by 4D LETKF on the
367 Kumagawa River flooding 2020. Progress in Earth and Planetary Science, 10(1), 1-22,
368 https://doi.org/10.1186/s40645-023-00537-3, 2023.
369 Köhne, J. M., Wöhling, T., Pot, V., Benoit, P., Leguédois, S., Le Bissonnais, Y., and Šimůnek, J.: Coupled
370 simulation of surface runoff and soil water flow using multi-objective parameter estimation. Journal of
371 Hydrology, 403(1-2), 141-156, https://doi.org/10.1016/j.jhydrol.2011.04.001, 2011.
372 Lee, J., Perera, D., Glickman, T., and Taing, L. Water-related disasters and their health impacts: A global
373 review. Progress in Disaster Science, 8, 100123, https://doi.org/10.1016/j.pdisas.2020.100123, 2020.
374 Li, M., and Yao, J.: Precipitation extremes observed over and around the Taklimakan Desert, China. PeerJ, 11,
375 e15256, https://doi.org/10.7717/peerj.15256, 2023.
376 Li, P. W., and Fan, C. M.: Generalized finite difference method for two-dimensional shallow water equations.
377 Engineering Analysis with Boundary Elements, 80, 58-71,
378 https://doi.org/10.1016/j.enganabound.2017.03.012, 2017.
379 Liu, Z., Zhang, H., and Liang, Q.: A coupled hydrological and hydrodynamic model for flood simulation.
380 Hydrology Research, 50(2), 589-606, https://doi.org/10.2166/nh.2018.090, 2019.
381 Merkuryeva, G., Merkuryev, Y., Sokolov, B. V., Potryasaev, S., Zelentsov, V. A., and Lektauers, A.:
382 Advanced river flood monitoring, modelling and forecasting. Journal of Computational Science, 10,
383 77-85, https://doi.org/10.1016/j.jocs.2014.10.004, 2015.
384 Merz, B., Blöschl, G., Vorogushyn, S., Dottori, F., Aerts, J. C., Bates, P., Bertola, M., Kemter, M., Kreibich,
385 H., Lall, U., and Macdonald, E.: Causes, impacts and patterns of disastrous river floods. Nature
386 Reviews Earth & Environment, 2(9), 592-609, https://doi.org/10.1038/s43017-021-00195-3, 2021.
387 Ming, X., Liang, Q., Xia, X., Li, D., and Fowler, H. J.: Real-time flood forecasting based on a

high-performance 2-D hydrodynamic model and numerical weather predictions. Water Resources Research, 56(7), e2019WR025583, https://doi.org/10.1029/2019WR025583, 2020.

Mori, K., Tada, K., Tawara, Y., Ohno, K., Asami, M., Kosaka, K., and Tosaka, H.: Integrated watershed modeling for simulation of spatiotemporal redistribution of post-fallout radionuclides: application in radiocesium fate and transport processes derived from the Fukushima accidents. Environmental Modelling & Software, 72, 126-146, https://doi.org/10.1016/j.envsoft.2015.06.012, 2015.

Najibi, N., and Devineni, N.: Recent trends in the frequency and duration of global floods. Earth System Dynamics, 9(2), 757-783, https://doi.org/10.5194/esd-9-757-2018, 2018.

Nanditha, J. S., Kushwaha, A. P., Singh, R., Malik, I., Solanki, H., Chuphal, D. S., Dangar, S., Mahto, S. S., Vegad, U., and Mishra, V.: The Pakistan flood of August 2022: Causes and implications. Earth's Future, 11(3), e2022EF003230, https://doi.org/10.1029/2022EF003230, 2023.

Petersen-Øverleir, A.: Modelling looped rating curves. In Proc., XXIV Nordic Hydrological Conf, pp. 139-146, https://doi.org/10.13140/2.1.1069.4403, 2006.

Ruidas, D., Saha, A., Islam, A. R. M. T., Costache, R., and Pal, S. C.: Development of geo-environmental factors controlled flash flood hazard map for emergency relief operation in complex hydro-geomorphic environment of tropical river, India. Environmental Science and Pollution Research, 30, 106951-106966, https://doi.org/10.1007/s11356-022-23441-7, 2022.

Sanders, B. F., Schubert, J. E., and Detwiler, R. L.: ParBreZo: A parallel, unstructured grid, Godunov-type, shallow-water code for high-resolution flood inundation modeling at the regional scale. Advances in Water Resources, 33(12), 1456-1467, https://doi.org/10.1016/j.advwatres.2010.07.007, 2010.

Sugawara, M.: The development of hydrological model-tank. Time and the River: essays by eminent hydrologists., 201-258, 1995.

Tellman, B., Sullivan, J.A., Kuhn, C., Kettner, A. J., Doyle, C. S., Brakenridge, G. R., Erickson, T. A., and Slayback, D. A.: Satellite imaging reveals increased proportion of population exposed to floods. Nature, 596, 80-86, https://doi.org/10.1038/s41586-021-03695-w, 2021.

Tradowsky, J. S., Philip, S. Y., Kreienkamp, F., Kew, S. F., Lorenz, P., Arrighi, J., ... and Wanders, N.: Attribution of the heavy rainfall events leading to severe flooding in Western Europe during July 2021. Climatic Change, 176(7), 90, https://doi.org/10.1007/s10584-023-03502-7, 2023.

Valente, M., Zanellati, M., Facci, G., Zanna, N., Petrone, E., Moretti, E., Barone-Adesi, F., and Ragazzoni, L.: Health system response to the 2023 floods in Emilia-Romagna, Italy: a field report. Prehospital and Disaster Medicine, 38(6), 813-817, https://doi.org/10.1017/S1049023X23006404, 2023.

Ward, P. J., Jongman, B., Kummu, M., Dettinger, M. D., Sperna Weiland, F. C., and Winsemius, H. C.: Strong influence of El Niño Southern Oscillation on flood risk around the world. Proceedings of the National Academy of Sciences, 111(44), 15659-15664, https://doi.org/10.1073/pnas.1409822111, 2014.

Wu, H., Chen, B., Ye, X. et al.: An improved calibration and uncertainty analysis approach using a multicriteria sequential algorithm for hydrological modeling. Scientific Reports, 11, 16954, https://doi.org/10.1038/s41598-021-96250-6, 2021.

Zhu, Y. L., Ishikawa, T., Subramanian, S.S., and Luo, B.: Simultaneous analysis of slope instabilities on a small catchment-scale using coupled surface and subsurface flows. Engineering Geology, 275, 105750, https://doi.org/10.1016/j.enggeo.2020.105750, 2020.

Zhu, Y. L., Zhang, Y. F., Yang, J., Nguyen, B. T., and Wang, Y.: A novel method for calculating distributed water depth and flow velocity of stormwater runoff during the heavy rainfall events. Journal of Hydrology, 612, 128064, https://doi.org/10.1016/j.jhydrol.2022.128064, 2022.